



A sustainable molybdenum oxysulphide-cobalt phosphate photocatalyst for effectual solar-driven water splitting



Naseer Iqbal^{a,*}, Ibrahim Khan^b, Asghar Ali^a, Ahsanullah Qurashi^{b,c}

^a Department of Chemistry, College of Science, University of Hafr Al Batin, PO. Box 1803, Hafr Al Batin 31991, Saudi Arabia

^b Center of Research Excellence in Nanotechnology, King Fahd University of Petroleum and Minerals, Dhahran 31261, Saudi Arabia

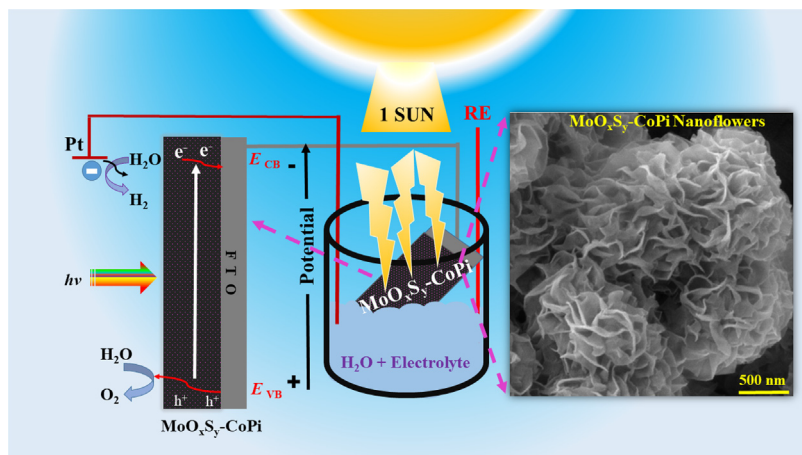
^c Department of Chemistry, Khalifa University of Science and Technology, Main Campus, Abu Dhabi, PO. Box 127788, United Arab Emirates

HIGHLIGHTS

- Facile synthesis of Molybdenum oxysulphide-cobalt phosphate ($\text{MoO}_x\text{S}_y\text{-CoPi}$) novel material for solar water splitting.
- The $\text{MoO}_x\text{S}_y\text{-CoPi}$ photocatalyst corresponded to the most stable oxidation states of Mo, Co, S, P, and O in the composite.
- Nanoflowers of $\text{MoO}_x\text{S}_y\text{-CoPi}$ showed controlled thickness up to ~ 10 nm, and variable interspaces of 200–400 nm were produced.
- Band-gap energy of 2.44 eV and significantly higher (7–8 folds) photocurrent density of $\text{MoO}_x\text{S}_y\text{-CoPi}$ is recorded compared to MoO_xS_y and CoPi.

GRAPHICAL ABSTRACT

A facile fabrication of $\text{MoO}_x\text{S}_y\text{-CoPi}$ photocatalyst revealed a conformal growth of nanoflowers. The photoelectrochemical studies exhibited significantly enhanced photocurrents with a stable and repeatable photocurrent response under visible light (1SUN) simulated solar irradiation.



ARTICLE INFO

Article history:

Received 9 November 2020

Revised 26 May 2021

Accepted 11 August 2021

Available online 13 August 2021

Keywords:

Photocatalysis

$\text{MoO}_x\text{S}_y\text{-CoPi}$ nanoflowers

Hydrothermal Reaction Synthesis

Water Splitting

ABSTRACT

Introduction: Hydrogen is considered as a clean alternative green energy future fuel. Since the Honda-Fujishima effect for photoelectrochemical water splitting is known, there has been a substantial boost in this field. Numerous photocatalysts based on metals, semiconductors, and organic-inorganic hybrid-systems have been proposed. Several factors limit their efficiency, e.g., a stable PEC-WS setup, absorbing visible light, well-aligned band energy for charge transfer, electrons and holes, and their separation to avoid recombination and limited water redox reactions. Metallic doping and impregnation of stable and efficient co-catalysts such as Pt, Ag, and Au showed enhanced PEC-WS. We used Cobalt-based co-catalyst with molybdenum oxysulfide photocatalyst for effectual solar-driven water splitting.

Objectives: To develop photocatalysts for efficient PEC processes capable of absorbing sufficient visible light, good band energy for effective charge transfer, inexpensive, significant solar-to-chemical energy

Peer review under responsibility of Cairo University.

* Corresponding author.

E-mail address: naseeriqbal@uhb.edu.sa (N. Iqbal).

<https://doi.org/10.1016/j.jare.2021.08.006>

2090-1232/© 2021 The Authors. Published by Elsevier B.V. on behalf of Cairo University.

This is an open access article under the CC BY-NC-ND license (<http://creativecommons.org/licenses/by-nc-nd/4.0/>).

conversion efficiencies. Above all, it is developing such PEC-WS systems that will be commercially viable for renewable energy resources.

Methods: We prepared Molybdenum oxysulphide-cobalt phosphate photocatalyst for PEC-WS through a facile hydrothermal route using ammonium heptamolybdate, thiourea, and metallic Cobalt precursors.

Results: An effectual photocatalyst is produced for solar-driven water splitting. The conformal morphology of $\text{MoO}_x\text{S}_y\text{-CoPi}$ nanoflowers is a significant feature, as observed under FE-SEM and HR-TEM. XRD confirmed the degree of purity and orthorhombic crystal structure of $\text{MoO}_x\text{S}_y\text{-CoPi}$. EDX and XPS identify the elemental compositions and corresponding oxidation states of each atom. A 2.44 eV band-gap energy is calculated for $\text{MoO}_x\text{S}_y\text{-CoPi}$ from the diffused reflectance spectrum. Photo-Electrochemical Studies (PEC) under 1-SUN solar irradiation revealed 7-8 folds enhanced photocurrent ($\sim 3.5 \text{ mA/cm}^2$) generated from $\text{MoO}_x\text{S}_y\text{-CoPi/FTO}$ in comparison to Co-Pi/FTO ($\sim 0.5 \text{ mA/cm}^2$) and $\text{MoO}_x\text{S}_y\text{-FTO}$ respectively, within 0.5 M Na_2SO_4 electrolyte (@pH=7) and standard three electrodes electrochemical cell.

Conclusion: Our results showed $\text{MoO}_x\text{S}_y\text{-CoPi}$ as promising photocatalyst material for improved solar-driven photoelectrochemical water splitting system.

© 2021 The Authors. Published by Elsevier B.V. on behalf of Cairo University. This is an open access article under the CC BY-NC-ND license (<http://creativecommons.org/licenses/by-nc-nd/4.0/>).

Introduction

Developing semiconducting nanomaterials for photoelectrochemical water splitting (PEC-WS) has gained substantial consideration [1–3] since the invention of the Honda-Fujishima effect [4,5]. Sunlight is a source of alternative energy, and its venture with photocatalytic nanomaterials can split water into molecular hydrogen and oxygen [6,7]. Lee et al. [8] and Wu et al. [9] illustrated photoelectrochemical solar water-splitting reaction consisting of an oxidation half-reaction, i.e., a multistep four-proton, four-electron process, which needs large overpotential to overawe the competing electron-hole recombination processes at the expense of solar-energy-conversion efficiency [8,10]. Significant research is carried out to investigate varieties of active photocatalytic materials [10–12]. Skment et al. reported Fe-O based semiconductors for PEC-WS applications [13], and L. Zhu et al. [14] prepared textured TiO_2/CuO composite nanofibers for enhanced solar H_2 generation. It is quite evident that such photocatalysts are aiding to achieve the escalating global energy demand and to discover sustainable energy resources [13–16]. However, further investigation is vital for an economical photocatalyst for PEC-WS. Developing a prolific photocatalysts needs, a stable PEC-WS setup, an efficient PEC processes that must be capable of absorbing a large fraction of the visible light, retain well-aligned band energy for thermodynamically promising charge transfer, and last but not least should be inexpensive [10,17]. Consequently, all characteristics mentioned above are requisite for effective photocatalyst for PEC-WS with significant solar-to-chemical energy conversion efficiencies to make these systems commercially viable.

Transition metal dichalcogenide, i.e., Molybdenum disulphide (MoS_2) and oxy-sulphides (MoO_xS_y) semiconducting nanomaterials [18,19] have been recently explored for PEC-WS. Owing to their enthralling electrical, optical, and catalytic properties, these nanomaterials are used to produce hydrogen and oxygen as alternative and sustainable green energy resources [20]. Different strategies, for instance, mechanical exfoliation [21], solution-based chemical exfoliation [22], chemical vapor deposition (CVD) [23], hydro and solvothermal synthesis [24], etc have been adopted to fabricate Molybdenum-oxy-sulphides (MoO_xS_y) and disulphide (MoS_2) photocatalysts. MoS_2 based nanomaterials are well-investigated for PEC-WS in comparison to MoO_xS_y photocatalysts. MoS_2 nanomaterials showed good electrical conductivity, i.e., charge carrier mobility $\geq 200 \text{ cm}^2/\text{V}^{\text{s}}$ in monolayer and up to $517 \text{ cm}^2/\text{V}^{\text{s}}$ in multilayers. Besides, their optical studies showed that MoS_2 exhibits a band-gap of $\sim 1.2 \text{ eV}$ – 2.2 eV in its monolayer and multilayers/bulk forms [25]. On the contrary, limited studies on Mo oxides or oxy sulphides are contained in the literature, likely because of solubility issues, mostly in acidic electrolytes and inadequate PEC characteristics. Nevertheless, Mayhall et al. [26], Sinaim et al. [27], and Xie et al.

[28] reported that incorporation of oxygen into Mo/MoS_2 greatly enhance the stability of the photocatalyst, limits its solubility, and improves the PEC properties of Mo based oxides and oxy sulphides. Therefore, our focus is to enhance those properties mentioned earlier for Mo, MoS_2 , and MoO_xS_y and their hybrid nanocomposites to be used as potential photocatalytic nanomaterials in solar cells and solar-driven PEC-WS applications [29].

In PEC-WS, hydrogen is generated following a hydrogen evolution reaction (HER). In such electrochemical reactions, the catalyst plays a decisive role in reducing the electrodes' overpotential that subsequently promote reaction efficiency. Likewise, the edges in 2-D Mo photocatalysts, i.e., MoS_2 and MoO_xS_y , the layered nanostructures and active sites located along with them, are coordinately unsaturated and thermodynamically unfavorable in addition to their basal surfaces that are chemically inert. These features correspond to their significant electrochemical properties [30]. Conversely, the utility of Mo based materials becomes limited in energy storage and conversion processes due to its high surface energy and strong interlayer π - π interactions that result in the restacking of layered nanostructures, hence showed poor stability, loss of active sites, and infrequent properties [31]. However, due to inadequate HER catalysts, there is an ongoing demand for substituting such nanomaterials and strategies. Recent research efforts have identified several attractive photocatalytic nanomaterials and molecular catalysts in photoelectrochemical (PEC) water splitting with numerous advantages. Despite its success, some factors in PEC hydrogen production need more improvements such as energy conversion efficiencies, limited charge recombination, and inefficient catalytic reduction and oxidation reactions. The incorporation of oxygen and a co-catalyst with Mo based compounds for both oxidation and reduction reactions have been used as an alternative approach to improve the photocatalytic activity of the nanomaterials in PEC-WS processes [32]. Among the co-catalysts, noble metal co-catalysts are well recognized, but the use of precious metals (Au, Ag, Pt, Pd) is not cost-effective. Hence this prompts the quest for alternative co-catalysts such as cobalt phosphate (CoPi). The literature revealed that cobalt phosphate (CoPi) significantly enhanced the PEC-WS properties in $1\text{D-WO}_3/\text{BiVO}_4$. That is attributed to a reduction in charge recombination, facilitating electron-hole transfer, and reducing the overpotential for OER in the water-splitting process [33].

Herein, based on the characteristics above for Mo, the significant role of oxygen incorporation into MoS_2 and support of Co-Pi as co-catalyst, we designed a novel Molybdenum oxysulphide-cobalt phosphate ($\text{MoO}_x\text{S}_y\text{-CoPi}$) photocatalyst for PEC-WS. Our research strategy has some intriguing features. Firstly, the novelty of the $\text{MoO}_x\text{S}_y\text{-CoPi}$ nanocomposite material in terms of its elemental composition and conformal growth of $\text{MoO}_x\text{S}_y\text{-CoPi}$

nanoflowers. Secondly, the ease and straightforward synthetic protocol, i.e., the in-situ growth of MoO_xS_y nanoflowers and cobalt phosphate (CoPi) co-catalysts in between MoO_xS_y layers. Last but not least, the cost-effectiveness in the fabrication of MoO_xS_y-CoPi, consolidating simple materials, and experimentation. In addition, our experiments showed that MoO_xS_y-CoPi/FTO enhanced the PEC signal by a factor of seven and eight in comparison to MoO_xS/FTO and Co-Pi/FTO photocatalysts, respectively. Therefore, considering the above traits, it is foreseen that this novel photocatalyst material will open new research directions to augment the challenges in solar-driven PEC-WS.

Experimental strategies

Materials and chemicals

The chemicals, reagents, and materials used in this study are of analytical grade and used as received unless otherwise stated. Ammonium heptamolybdate tetrahydrate, Thio-urea, cobalt powder, phosphoric acid (85%), ammonia solution, sodium sulfate (Na₂SO₄), ethanol and acetone are purchased from Sigma Aldrich. We used deionized water in all experiments.

Synthesis of nanomaterials

Synthesis of cobalt phosphate (CoPi)

CoPi synthesis is carried out from metallic cobalt powder and phosphoric acid (85%). The equimolar reaction mixture is sonicated at 50 °C continuously with the dropwise addition of 10 ml deionized water at the rate of 2 ml/10 min. After the complete addition of deionized water, the reaction mixture is sonicated for a further half an hour at 60 °C and then cooled to room temperature. In the next step, 25% ammonia solution (5 ml or as required) is added to initiate precipitation, while maintaining pH at 13. Later on, the reaction mixture is transferred into a stainless steel autoclave containing Teflon vessel. The solvothermal reaction has proceeded for 6 h at 200 °C. Afterward, the reaction mixture is centrifuged at 4000 RPM for 5 min. The violet color product collected and washed with deionized water several times to remove undesired and unreacted moieties before drying in a vacuum oven for 2 h at 150 °C.

Synthesis of molybdenum oxysulfide-Cobalt phosphate nanocomposite (MoO_xS_y-CoPi)

The equimolar amounts of ammonium heptamolybdate and thiourea mixed in deionized water are stirred to obtain a clear mixture. In this mixture, an equimolar amount of as prepared CoPi is added slowly with continuous stirring. The reaction mixture is placed in an ultrasonic bath for one hour at 60 °C to acquire homogeneous mixing. The reaction mixture is transferred into a stainless steel autoclave containing a Teflon vessel to proceed with a hydrothermal reaction for 24 h at 180 °C. Afterward, the reaction mixture containing precipitates of MoO_xS_y-CoPi is centrifuged at 4000 RPM for 5 min, washed with ethanol and acetone, respectively, before drying in a vacuum oven at 200 °C for two hours. Finally, the MoO_xS_y-CoPi photocatalyst nanomaterial is annealed at 400 °C for 4 h in the air.

Synthesis of molybdenum oxysulfide (MoO_xS_y)

MoO_xS_y is prepared by the same strategy as mentioned above in section-b but without Co-Pi. The purpose of MoO_xS_y synthesis is only to study and compare its morphology and PEC properties with MoO_xS_y-CoPi and CoPi.

Characterization of nanomaterials

The purity and crystalline phases of MoO_xS_y-CoPi nanoflowers and CoPi are characterized by X-ray diffraction (XRD) technique

using a Benchtop MiniFlex -X-ray Diffraction instrument (Mini-XRD) from Rigaku (40 kV and 15 mA) in the range of 10–70° (2θ) at a scanning rate of 3° min⁻¹ with CuK alpha radiation. The structural composition and crystalline phases prevailing in MoO_xS_y-CoPi nanoflowers and CoPi are interpreted with library data. Also, the elemental composition and oxidation states of metals involved during MoO_xS_y-CoPi formation are verified by X-ray photoelectron spectroscopy (XPS) using PHI 5000 Versa Probe II spectrometer (UIVAC-PHI), employing Al Kα as the incident radiation source. The C1s (E = 284.5 eV) level served as the internal standard. The morphology of the MoO_xS_y-CoPi nanoflowers, MoO_xS_y, and CoPi is observed under TESCAN Lyra 3 Field Emission Dual Beam (Electron/ Focused Ion Beam) system combined with high-end field-emission scanning electron microscope (FE-SEM). This machine is also facilitated with EDX for elemental determination/mapping. HR-TEM study is carried out via (JEM2100F, JEOL at 200 kV) imaging to comprehend the MoO_xS_y and CoPi interfaces formed in the composite nanoflowers. Optical properties, i.e., diffused reflectance spectroscopy of MoO_xS_y-CoPi nanoflowers and CoPi, are carried out using Agilent Cary 5000 high-performance UV-Vis-NIR spectrophotometer containing praying mantis accessory with alignment tools and powder cell sample cups. In situ Raman spectroscopy of MoO_xS_y-CoPi nanoflowers and CoPi was performed with a laser (300 mW Green 532 nm) by iHR-320 Horiba imaging spectrometer. The vibrational modes in the MoO_xS_y-CoPi nanoflowers and CoPi are recorded by FT-IR 6700 Nicolet™ FT-IR spectrometer. A fluorolog-3 imaging spectrophotometer tests the photoluminescence activity of the nanomaterials at an excitation wavelength of 350 nm and a slit width of 2 nm.

Fabrication of MoO_xS_y-CoPi/FTO, MoO_xS_y/FTO, and CoPi/FTO photocatalysts for PEC

Studies

Fluorinated Tin Oxide (FTO) conducting glass substrates are used for photoelectrochemical studies of MoO_xS_y-CoPi and CoPi. Initially, FTO glass substrates are washed by acetone (10 min) and water (10 min), respectively, with continuous ultrasonication. In the next step, slurries of MoO_xS_y-CoPi nanoflowers, MoO_xS_y, and CoPi from 0.25 g of the materials are prepared in ethanol/water (70%/30%) mixture and coated over pre-treated FTO glass substrates by drop-casting, respectively. The optimized film is highly uniform and completely covered the desired area of the FTO substrate. The MoO_xS_y-CoPi/FTO, MoO_xS_y/FTO, and CoPi/FTO electrode were heated at 110 °C for 2 h to evaporate the solvents and harden the MoO_xS_y-CoPi nanoflowers and CoPi layers so that they could withstand during the PEC measurements. The PEC measurements are carried out by a three-electrode system in 0.5 M Na₂SO₄ (pH = 7) solution, where a Pt wire served as a counter electrode. The FTO coated MoO_xS_y-CoPi nanoflowers, and CoPi substrates served as photocatalysts or working electrodes, and the standard calomel (SCE) as a reference electrode. The PEC measurements are performed by Metrohm Autolab Potentiostat (PGSTAT302N). Moreover, for simulated solar light, we utilized Oriol sol 3A class AAA Solar Simulator-Newport (100 mW.cm⁻²) IEC/JIS/ASTM certified containing 450Watt Xenon lamp, Air Mass 1.5G Filter, and 2x2 inch aperture for output beam.

Results and discussions

FE-SEM & HR-TEM studies of MoO_xS_y-CoPi and CoPi nanomaterials

The surface studies of MoO_xS_y, CoPi, and MoO_xS_y-CoPi nanocomposite are carried out via the FE-SEM technique, as shown in Figs. S1-A, S1-1B (In supplementary information), and Fig. 1 respectively. The solid MoO_xS_y shows distorted nanorods or flakes like growth, supported in literature through a different synthesis

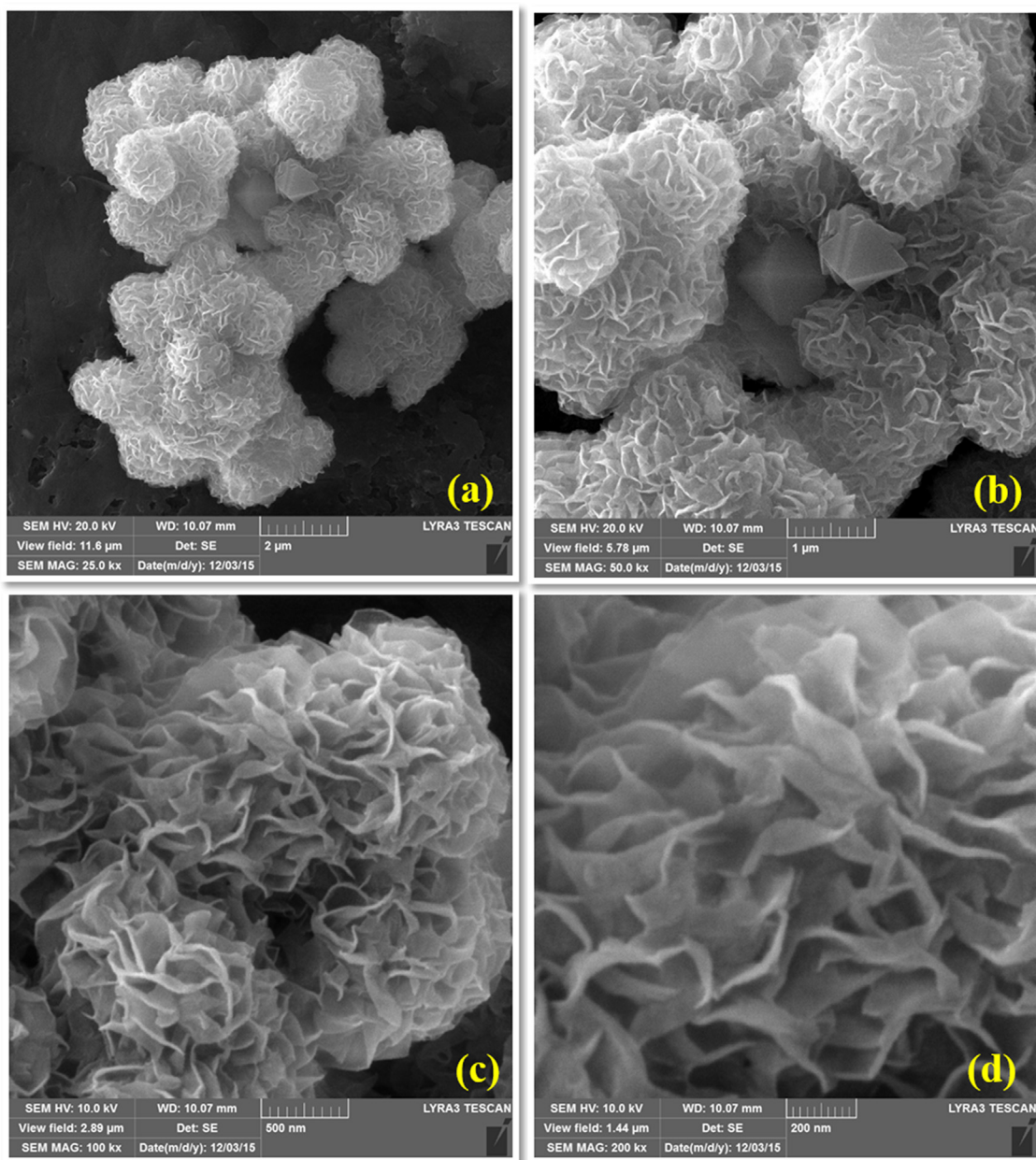


Fig. 1. SEM micrographs of $\text{MoO}_x\text{S}_y\text{-CoPi}$ composite nanoflowers. Where (a) & (b) are low-resolution micrographs, showing the appearance of uniform nanoflowers of $\text{MoO}_x\text{S}_y\text{-CoPi}$. (c) & (d) high resolution FE-SEM images of $\text{MoO}_x\text{S}_y\text{-CoPi}$.

[34,35]. The nanomaterial (MoO_xS_y) is synthesized by the same procedure as adopted for the $\text{MoO}_x\text{S}_y\text{-CoPi}$, i.e., the hydrothermal synthesis. However, the morphology of MoO_xS_y differs from what we observed for $\text{MoO}_x\text{S}_y\text{-CoPi}$ at the same reaction conditions. Similarly, the FE-SEM of bare CoPi revealed particulate morphology, with EDS, indicated the constituent elemental ratios (Figs. S2 & S3) in a good agreement. Fig. 1 (a,b) and (c,d) show low and high-resolution micrographs of $\text{MoO}_x\text{S}_y\text{-CoPi}$ nanoflowers. The $\text{MoO}_x\text{S}_y\text{-CoPi}$ exhibit a uniform nanoflowers like morphology, with controlled nanosheets thickness, variable internal spaces, and good crystallinity (as supported by XRD studies). Under high magnification FE-SEM, the nanoflower growth of MoO_xS_y is observed with CoPi incorporation within the flakes of MoO_xS_y as a result of the hydrothermal reaction by taking equimolar amounts of both precursors. While looking at Fig. 1d, the thickness of the curved nanopetals in $\text{MoO}_x\text{S}_y\text{-CoPi}$ nanoflowers can be estimated, which ranges beyond 10 nm. However, the internal distances between

curved channels show variation between 200 and 400 nm. To further confirm, we performed energy dispersive spectroscopy (EDS) and transmission electron microscopy (TEM) analysis. Fig. 2 shows the EDS spectrum performed at different sites of the $\text{MoO}_x\text{S}_y\text{-CoPi}$ composite nanoflowers with their corresponding atomic ratios that substantiated significant atomic ratios of Mo, Co, S, O, and P, respectively. Thus it is confirmed the equimolar amounts of both the precursors resulted not only in optimal material growth but also showed enhanced PEC-WS properties.

The TEM was performed to confirm the dispersion of CoPi within the channels of MoO_xS_y nanoflowers supported by high angle annular dark-field (HAADF) scanning transmission electron microscopy (STEM). Two different morphologies corresponded to MoO_xS_y and CoPi can be seen in the higher magnification TEM image in Fig. 3a. Likewise, Fig. 3b presents an evaluation of the blue cross-section via HRTEM elucidating two kinds of d-spacing patterns that are usually characteristics of nanocomposite materials

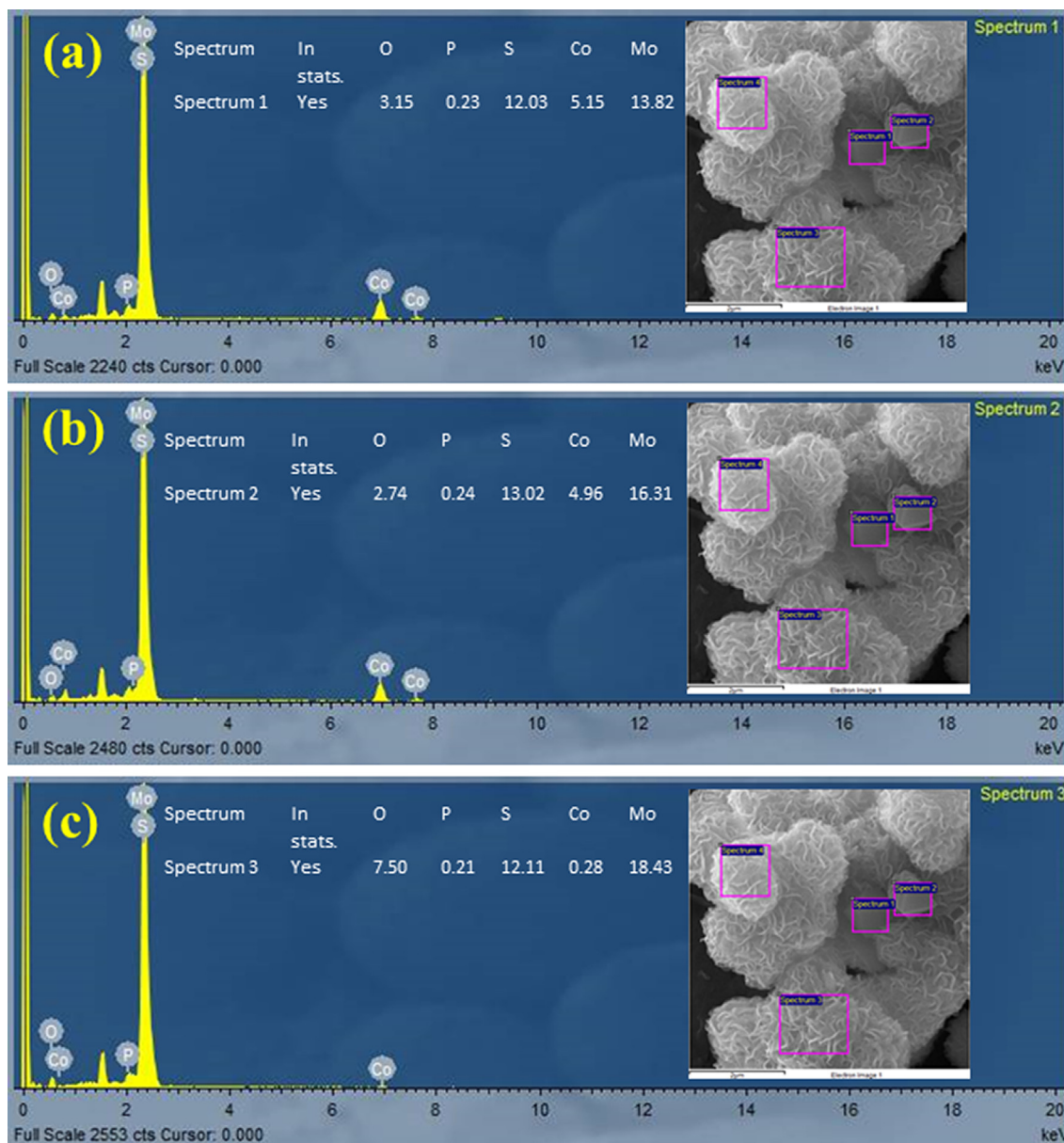


Fig. 2. EDS studies of MoO_xS_y-CoPi nanoflowers a single-phase composite material fabricated @ 2 h at 180°C via a hydrothermal route (a), (b) & (c) present EDS spectrums with corresponding elemental peaks for Mo, Co, S, P, and O respectively. The onset SEM micrographs present element distribution images of MoO_xS_y-CoPi as well as atomic ratios of Mo, Co, S, P, and O.

with good crystallinity. Fig. 3 (c & e) shows high resolution (HR)-TEM micrograph, the Fast-Fourier transform (FFT) micrographs further demonstrate the MoO_xS_y-CoPi nanoflower composite formation. It is evident from these micrographs that the MoO_xS_y exhibit larger d-spacing (0.56 nm) than CoPi (0.28 nm). The linear EDX spectra agree with EDX obtained from FESEM (Fig. S4 in supplementary information). Thus, the HR-TEM studies provided ample evidence for the successful formation of MoO_xS_y-CoPi nanocomposite.

X-Ray diffraction (XRD) analysis

X-ray diffraction analysis is performed to explore the crystal structure and the degree of purity of CoPi and MoO_xS_y-CoPi nanostructures. It revealed that MoO_xS_y-CoPi materials have a polycrystalline structure with orthorhombic crystalline phases. XRD patterns of MoO_xS_y-CoPi and CoPi nanostructures are shown in

Fig. 4. Both MoO_xS_y-CoPi and CoPi display diffraction peaks of MoO_xS_y and CoPi at their corresponding indexes through matching with the library data under JCPDS card No. 65-2421 and 01-078-6161. The XRD pattern of MoO_xS_y-CoPi matches with MoO₃ pattern, suggesting that most of the sulfur is replaced by oxygen during annealing. The CoPi showed peak intensities at 2θ angle are ~18,21,26,31,36,39,42,45,52,55 and 57 with corresponding indexes observed at (200), (101), (201), (211/020), (200), (220), (102), (202), (212), (131), (231) and (412), respectively. The sharp and high intensities diffraction peaks exposed the formation of high crystalline orthorhombic CoPi that is also supported by various literature studies [36,37]. The XRD spectra of MoO_xS_y-CoPi composite presented in Fig. 4 have main diffraction peaks at ~13,24,26,28,39,46,49 with corresponding indexes at (020/200), (110/101), (040), (021/201), (060/600), (002) respectively, which are in correspondence to MoO₃. Some CoPi diffraction peaks at ~18,21,31,36,42 with corresponding indexes at (200), (101),

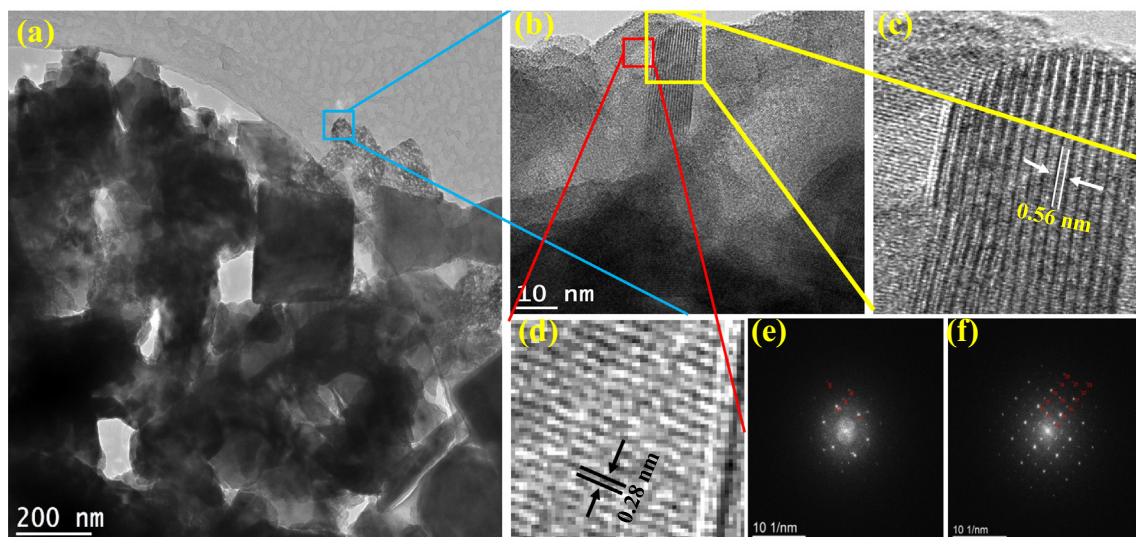


Fig. 3. TEM analysis of MoO_xS_y-CoPi nanocomposite: (a) and (b) show the lower and higher magnification TEM, (c) and (f) correspond to d spacing pattern of MoO_xS_y and, (d) and (e) corresponds to d spacing pattern of CoPi.

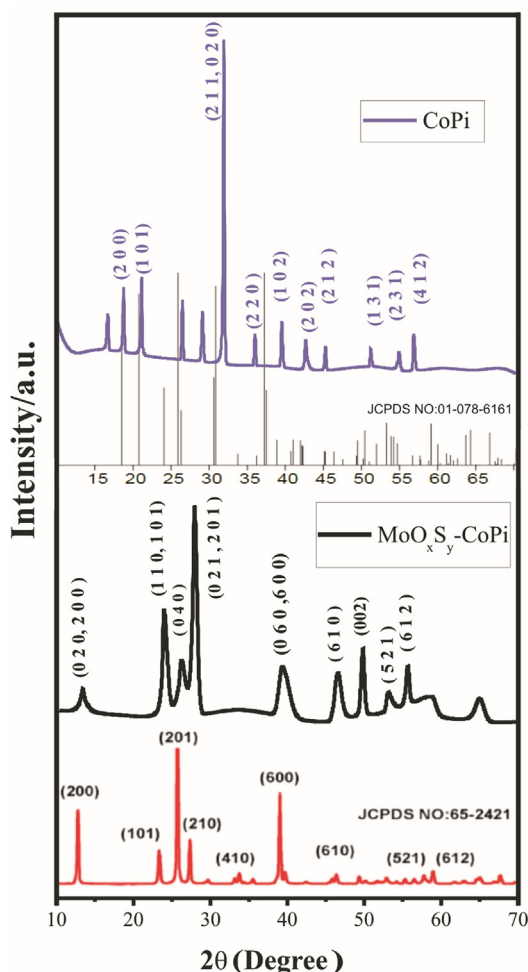


Fig. 4. XRD patterns of MoO_xS_y-CoPi (Black) and CoPi (purple) showing 2θ peak angles and their corresponding indexes (JCPDS card No. 65-2421 and 01-078-6161).

(211/020), (220), (202) either completely disappeared or shifted into broad peaks in the MoO_xS_y-CoPi composite. Most likely, it is due to new chemical interactions established between MoO_xS_y

and CoPi. The role of effective ionic radii [38] cannot be ignored: elements of nearly close ionic radii in different oxidation states like Mo & Co and O & S can develop new chemical interactions and phases during the composite formation. Considering this, the appearance of some new crystal phases at peak intensities 2θ = 28 (021/201) and broad peaks at 2θ = 13(020/200), 24 (110/101) & 46 (060/600) endorses the formation of MoO_xS_y-CoPi nanocomposite material.

The XRD patterns of MoO_xS_y-CoPi also showed three characteristic MoO_x diffraction peaks at 2θ angles ~13, 26, and 39 corresponding orthorhombic crystalline phase indexes (020), (040), and (060/600), respectively [18,39]. The slight shifting in these peaks is attributed to the formation of new composite material and the synthetic strategy adopted. In summary, the XRD patterns of MoO_xS_y-CoPi showed some new and combined peaks that arose due to the possible existence of sulfur contents and also the composite formation of MoO_xS_y with CoPi via a hydrothermal approach.

X-Ray photoelectron spectroscopy

The elemental composition of MoO_xS_y-CoPi composite and their corresponding oxidation states are investigated by X-ray photoelectron spectroscopy (XPS). The spectrums are presented in Fig. 5. A complete elemental XPS survey indicated the presence of Mo, S, Co, P, and O elements (Fig. 5a), which are present in the MoO_xS_y-CoPi and found in good agreement with the EDX and TEM findings. This not only comprehended the formation of MoO_xS_y-CoPi nanoflower composite but also supported the *in-situ* impregnation of CoPi in MoO_xS_y layers during a hydrothermal reaction. All the peaks are adjusted with the reference C 1s peak (284.6 eV) before further description. Fig. 5b shows the Mo (3d) spectra consisting of two spin-orbit triplet peaks characteristics of Mo-S (3d_{5/2}), Mo-S (3d_{3/2}), and a residual Mo-O (3d), respectively [18]. These Mo (3d) components at ~229.7 eV, 232.5 eV, and 235.5 eV can be assigned as Mo⁺⁴, Mo⁺⁶ and Mo⁺² oxidation states, respectively. The occurrence of reduced Mo oxidation states indicate that the d-orbital is partially filled; therefore, it showed the enhanced electrical conductivity [24], as can be seen in PEC-WS. Likewise, the S (2p) spectra, as presented in Fig. 5c, contains residual peaks with two dominant spin-orbit doublets, i.e., characteristics of S²⁻ 2p_{3/2} at 161.8 eV and S²⁻ 2p_{1/2} at 164.2 eV, respectively,

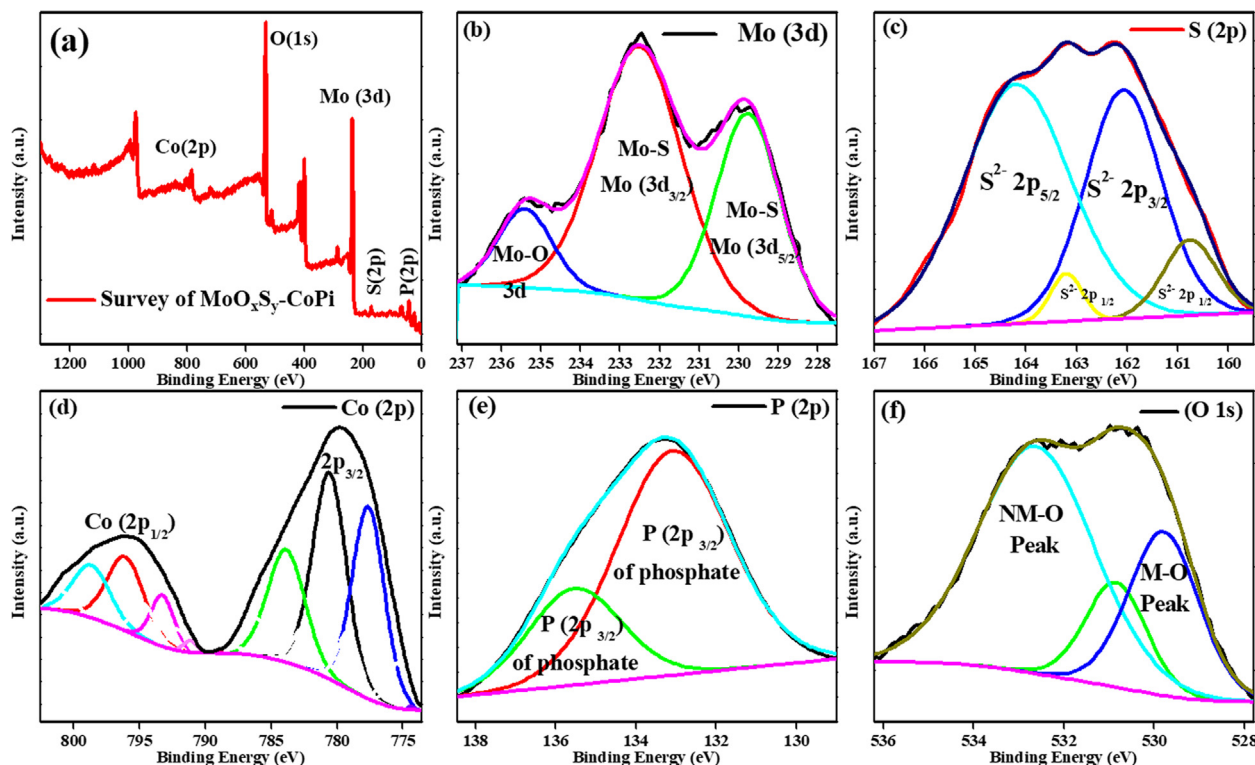


Fig. 5. XPS spectra of the constituent elements of $\text{MoO}_x\text{S}_y\text{-CoPi}$ nanoflowers, where (a) shows complete elemental XPS survey indicated the presence of Mo, S, Co, P, and O elements, (b) shows the Mo (3d) spectra consisting of two spin-orbit triplet peaks characteristics of Mo-S ($3d_{3/2}$), Mo-S ($3d_{5/2}$), and a residual Mo-O (3d), respectively, (c) contains residual peaks with two dominant spin-orbit doublets $\text{S}^{2-} 2p_{3/2}$ & $\text{S}^{2-} 2p_{5/2}$, (d) elaborates XPS spectra of Co doublet 2P splitting, i.e., $2p_{3/2}$ and $2p_{1/2}$, (e) displays the P (2p) spectra that exhibit characteristic $2p_{3/2}$ doublets of Phosphorous and (f) demonstrates the spectra of O (1 s), i.e., low energy metal-oxygen (M-O) and higher energy nonmetal-oxygen (NMO) photoelectron peaks.

which specifies that Sulphur exists as a very stable oxidation state, i.e., (-2) in the $\text{MoO}_x\text{S}_y\text{-CoPi}$ composite material [24]. However, some lower intensity doublet peaks characteristic of $\text{S}^{2-} 2p_{1/2}$ at 160.7 eV and 163.2 eV correspond to further oxidation of Sulphur in the MoO_xS_y composite [40]. Benoist et al [40] reported a similar environment of Sulphur in MoO_xS_y films. In light of their study, the S 2p peaks are split up into four components (160.7 eV, 161.8 eV, 163.2 eV, and 164.2 eV), as shown in Fig. 5c. The binding energies of these doublets are close to those determined for the S 2p peak of the sulfur-rich thin films having the composition and environment similar to that of MoS_2 , this sulfur is obviously S^{2-} , the real effective charge of which is more negative than the actual charge of S^{2-} in MoS_2 . It is also observed that when the amount of oxygen increases in MoO_xS_y , the central doublet peak (163.2 eV) decreases. However, the doublets at higher and lower binding energies (peaks at 164.2 eV and 161.9 eV) equally increase (Fig. 5c). Thus, both sulfur and oxygen ions are associated with the new species of molybdenum oxy sulphide. Benoist et al [40] confirmed that their XPS data showed new “oxysulfide” in which molybdenum environment is composed of oxygen (O^{2-}) and sulfur (S^{2-}) in equal proportions. Their findings were also aligned with electron spin resonance (ESR) studies conducted by Deroide et al. [41,42] for molybdenum sulphide compounds.

The XPS data presented in Fig. 5 (c & d) disclosed an interesting observation; the spectra concluded that MoO_xS_y and CoPi remain intact in the $\text{MoO}_x\text{S}_y\text{-CoPi}$ nanoflower composite material [18]. Fig. 5 (d) further elaborates on the XPS insights of CoPi in $\text{MoO}_x\text{S}_y\text{-CoPi}$ nanocomposite material. The XPS spectra of Co demonstrate a doublet of 2P splitting, i.e., $2p_{3/2}$ and $2p_{1/2}$ peaks with analogous shakeup satellites peaks, i.e., each splitting correspond to three spectral lines. Thus the Co ($2p_{3/2}$) spectral lines observed at 777.9 eV, 781 eV, and 784 eV can be assigned to Co, Co-O, and

Co-P [43–45], respectively. However, Co ($2p_{1/2}$) spectral lines observed at 793.0 eV, 796 eV, and 799 eV can be assigned to Co, Co-O, and Co-O(sat) [44,46], respectively. Fig. 5 (e) displays the P (2p) spectra that exhibit characteristic $2p_{3/2}$ doublets of Phosphorous. It consists of photoelectron lines at 133.0 eV and 135.8 eV conforming to its most stable oxidation state (+5) in the phosphate group ($-\text{PO}_4$). [47,48] within the $\text{MoO}_x\text{S}_y\text{-CoPi}$ nanocomposite. Lastly, Fig. 5 (f) demonstrates the spectra of O (1 s); low energy metal-oxygen (M-O) photoelectron peaks corresponding to

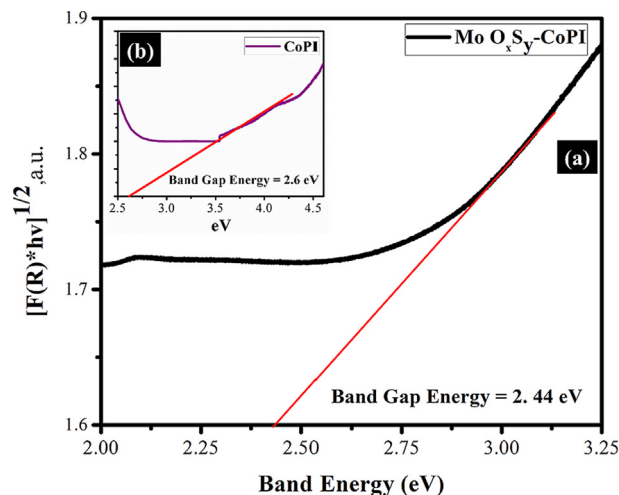


Fig. 6. Band energy estimation (a) diffused reflectance spectrum for band-gap estimation of $\text{MoO}_x\text{S}_y\text{-CoPi}$ nanoflowers (b) diffused spectrum for band-gap calculation of CoPi.

529.5 eV, and 531 eV, i.e., for Mo–O and Co–O, respectively. Furthermore, a higher energy nonmetal-oxygen (NMO) photoelectron peak corresponding at > 531 eV, i.e., for O–S and O–P, which can be attributed to the phosphate-oxygen and adsorbed moisture, i.e., O–H bond [49,50]. These XPS findings confirm that MoO_xS_yn and CoPi retained their chemical identity in the MoO_xS_y-CoPi nanocomposite, as the binding energy of the constituent elements agrees with reported values for MoS₂ and CoPi, markedly [18].

Optical properties of CoPi and MoO_xS_y-CoPi nanomaterials

UV–VIS spectroscopy and bandgap

Diffused reflectance spectra of pure MoO_xS_y-CoPi and CoPi are presented in Fig. 6. Their optical properties are investigated using Cary 4000 series UV–VIS–NIR spectrophotometer. The blend of CoPi within MoO_xS_y nanostructure changes the optical characterization of the nanocomposite material. The band-gap energy of CoPi (inset plot in Fig. 6) is estimated from the diffused reflectance spectrum, and it is found to be ~2.6 eV. The literature revealed MoS₂ and MoO_x exhibit band-gap energies ~1.2–2.2 eV in its monolayer and multilayer/bulk form, respectively [25]. In our studies, the band-gap energy observed for MoO_xS_y-CoPi composite from Tauc's Plot method [51,52] is 2.44 eV, as can be perceived in Fig. 6 (a). A noticeable difference in the band-gap energies from CoPi and MoO_xS_y is observed. This shift in band gap energies could be attributed to changing phase and crystal structure upon the incorporation of CoPi to MoO_xS_y. Besides several factors such as morphology, variation in crystallographic phases and structure, particle size, annealing temperature, etc. can influence the optical properties of semiconducting materials [53].

Vibrational spectroscopy

FTIR-Spectroscopy

The structural properties of MoO_xS_y-CoPi and CoPi are further expounded via Raman and FTIR spectroscopy. The FT-IR analysis of both CoPi and MoO_xS_y-CoPi nanoflowers composite material are presented in Fig. S5-A and S5-B respectively of [supplementary information](#). The FT-IR for CoPi showed peaks at vibrational frequencies 620 cm⁻¹, 755 cm⁻¹, 860 cm⁻¹, 1050 cm⁻¹, 1440 cm⁻¹, 1650 cm⁻¹, 2750 cm⁻¹, 3240 cm⁻¹ and 3380 cm⁻¹. These peaks are in good agreement to the reported FT-IR for CoPi in literature [36,54,55] i.e., 605 cm⁻¹, 956 cm⁻¹, 1008 cm⁻¹, 1045 cm⁻¹, 1632 cm⁻¹, 2930 cm⁻¹ and 3450 cm⁻¹. The most plausible reason of this shifting is the synthetic strategy and morphology of the material synthesized. On the other hand MoO_xS_y-CoPi shows IR peaks at 510 cm⁻¹, 780 cm⁻¹, 860 cm⁻¹, 960 cm⁻¹, 1080 cm⁻¹, 1140 cm⁻¹, 2015 cm⁻¹, 2255 cm⁻¹, 3120 cm⁻¹ and 3240 cm⁻¹ respectively. These bands corroborate with the characteristics peaks of both MoOS₂ [56–59] and CoPi at their respective vibrational modes as reported in the literature [36,54,55]. The IR band at 510 cm⁻¹ corresponds to ν_{as} (Mo–S) vibrations. However, the bands above 600 cm⁻¹ correspond to Mo–O type of vibrations due to reaction presence of oxygen in the Mo–S–O, thus different peaks as labeled in Fig. S5-B indicate that oxygen is present in similar types of coordination environment as observed for MoO₃ [56]. We allocated the bands at 860 cm⁻¹ and 960 cm⁻¹ to the ν_{as}(Mo–O) vibrations and 780 cm⁻¹ to ν (Mo–O) vibrations. Some IR peaks observed in CoPi or MoO_xS_y, respectively either disappeared or shifted to lower intensities and some become intense and sharp in MoO_xS_y-CoPi. This shifting of IR bands is attributed to formation of new composite that is mainly depending upon the synthetic methodology adopted, crystalline phases and morphology.

Raman spectroscopy

The Raman spectrum indicates characteristic phononic peaks in the fingerprint regions from 0 cm⁻¹ to 1200 cm⁻¹. Fig. S5-C in [supplementary information](#), presents the Raman scattering of both MoO_xS_y-CoPi (red color line) and CoPi (blue color line), respectively. All the peaks are assigned according to their modes of vibrations comparable with the literature [60,61]. The vibrational peaks for CoPi are observed in region 50–200 cm⁻¹ and 940 cm⁻¹, respectively. However, these peaks appeared sharper and intense after hydrothermal reaction for MoO_xS_y-CoPi formation, i.e., peaks recorded at 50 cm⁻¹, 100 cm⁻¹, 140 cm⁻¹ and 980 cm⁻¹, respectively. Furthermore, the characteristics Raman scattering of MoO_xS_y in MoO_xS_y-CoPi nanoflowers composite are shifted to lower values, i.e., the phononic peaks observed at 310 cm⁻¹ (E_{2g}) and 355 cm⁻¹ (A_{1g}), respectively. These peaks are assumed to be first-order Raman vibration modes within S–Mo–S layers [61]. Also, the appearance of new sharp and broad phononic peaks at 225 cm⁻¹, 260 cm⁻¹, 650 cm⁻¹ and 800 cm⁻¹ are considered due to interactions between MoO_xS_y and CoPi atoms, e.g., P–Co–S or P–Mo–S or O atom to P, S, and Mo or vice versa. Nonetheless, the vibrational studies authenticate the formation of MoO_xS_y-CoPi that have potential photoelectrochemical applications.

Photoluminescence's spectroscopy

Photoluminescence (PL) spectroscopy of MoO_xS_y-CoPi and CoPi is carried out at room temperature with an excitation wavelength of 350 nm, as described in Figs. S6-A and S6-B in [supplementary information](#), respectively. Fig. S6-B presents the first onset of the PL curve, which lies in a visible light region with PL peak maxima observed at ~425 nm. The onset initiates at 370 nm (~3.35 eV) and prolonged till 550 nm (~2.26 eV) as of Fig. S6-B (blue line baseline fitted PL spectrum). The maximum excitation is observed at ~425 nm (~2.92 eV) in the MoO_xS_y-CoPi. However, this peak for CoPi (Fig. S6-A in [Supplementary information](#)) is recorded between 410 and 420 nm (~3.03 eV–2.95 eV). This small shift of PL peak for CoPi in MoO_xS_y-CoPi is attributed to the appearance of some defects and crystalline phases in the growing MoO_xS_y-CoPi during the hydrothermal reaction. The PL spectra also displayed low-intensity peaks between 580 and 680 nm, as shown in Fig. S6-B (red PL spectra in onset). This broader peak corresponds to MoO_xS_y as a result of direct excitonic transitions (A1 and B1) in the range of 620–650 nm (2.0–1.9 eV). These excitations are following the literature values [61,62], where A1 and B1 transitions are recorded at 630 nm and 670 nm (1.97 eV– 1.85 eV), respectively. The shifting of PL emission peaks for CoPi and MoO_xS_y in our synthesized MoO_xS_y-CoPi nanomaterials are attributed to slower electronic relaxation. Furthermore, this shifting could be due to crystalline structure and nanoflowers like morphology of MoO_xS_y-CoPi as compared to CoPi and MoO_xS_y, independently. The presence of structural defects on the surface of nanopetals of MoO_xS_y-CoPi nanoflowers composite materials is also responsible for different PL spectra. That ultimately enhanced the disordered arrangement among Mo, Co to Sulphur, oxygen, and phosphorus and shifted excitations little away from the band-gap energies [61,62].

Photoelectrochemical performance of MoO_xS_y-CoPi, MoO_xS_y, and CoPi Photocatalysts

Chronoamperometry

MoO_xS_y-CoPi/FTO, MoO_xS_y/FTO, and CoPi/FTO Photocatalysts are prepared and used for PEC measurements in a standard three-electrode electrochemical cell. The cell contains an FTO coated working electrode, a reference standard calomel electrode (SCE), and a platinum counter electrode in 0.5 M Na₂SO₄ electrolyte solution at neutral pH (7). The photoresponse of each photocatalyst

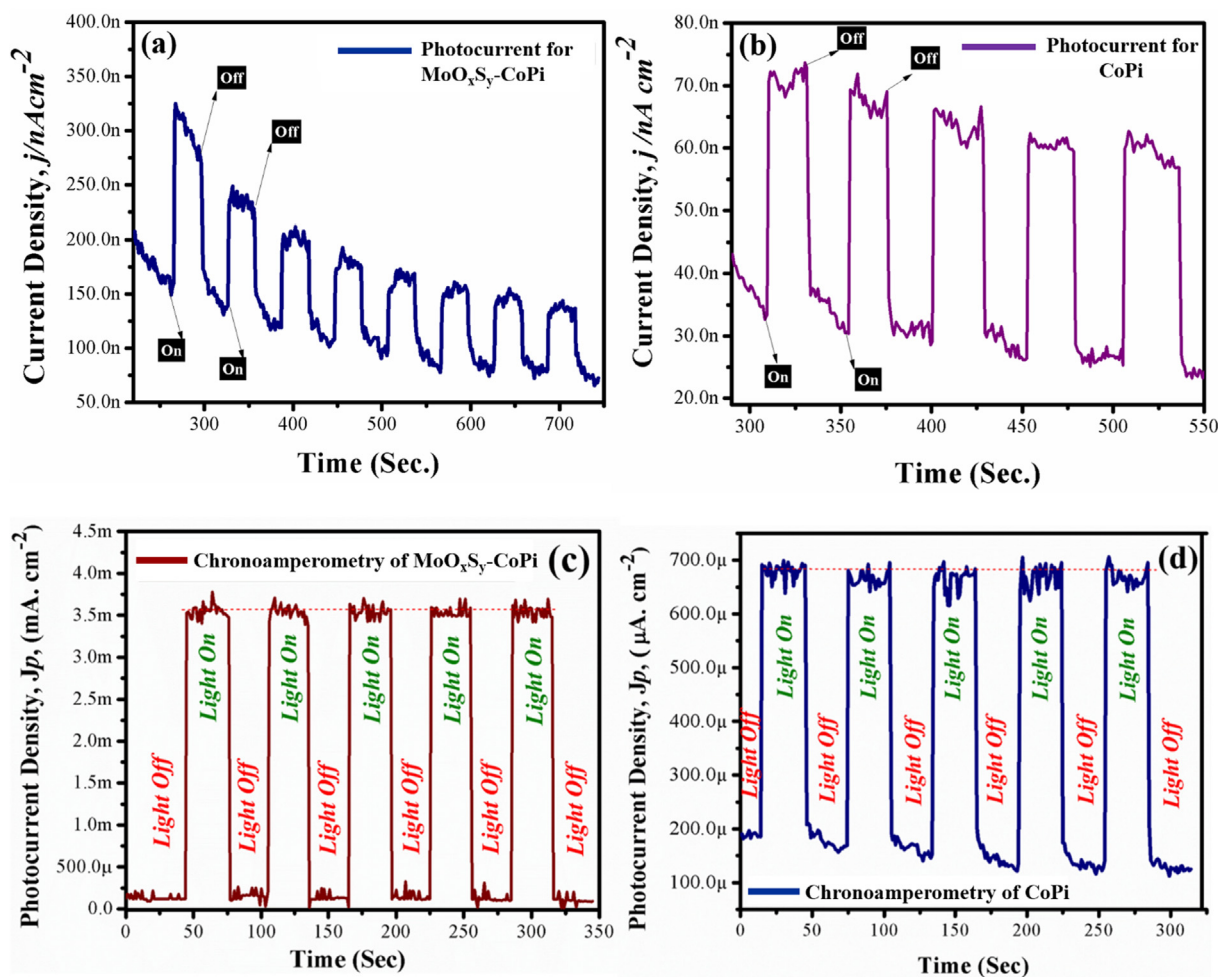


Fig. 7. Chronoamperometric measurements of MoO_xS_y-CoPi (a & c) and CoPi (b & d) at applied potentials of 0 V and 0.2 V respectively.

exposed to 1 SUN light source is recorded after regular intervals of time. The chronoamperometric measurements are presented in Fig. 7(a-d), which shows photocurrent density vs. time (J_p vs. t) profiles. The photocurrent generated from MoO_xS_y-CoPi/FTO photocatalyst is in the range of nano amperes, i.e., ~150 nA at the at ~0.0 V. This is 4–5 times higher than photocurrent observed for CoPi at ~0.0 V (Fig. 7b), which is only ~30 nA. We further extended our chronoamperometry studies at higher applied potentials. Fig. 7 (c & d) shows chronoamperometry measurements of both CoPi and MoO_xS_y-CoPi at 0.2 V applied potential. Fig. 7c presents the highest photocurrent density, i.e., 3.5 mA.cm⁻² from MoO_xS_y-CoPi nanoflowers composite. A photoresponse further explicit significant stability of MoO_xS_y-CoPi coated on FTO over a longer period. A stability measurement for MoO_xS_y-CoPi/FTO photocatalyst further confirms this recital upon continuous exposure to 1 SUN solar simulated light without any significant degradation within a given time, as shown in Fig. S7 (supplementary information). The photocurrent density recorded from CoPi is in the range of 500 μA.cm⁻² as of Fig. 7d. While performing PEC measurements for both MoO_xS_y-CoPi nanoflowers composite material and CoPi, we exhibited reversible response profiles with adequate stability in ON/OFF light modes. That, in turn, reflects the successful performance of MoO_xS_y-CoPi nanoflowers composite material for water splitting processes. The linear sweep voltammetry experiments further complimented this efficient PEC performance, where the photocurrent density is enhanced to mA, i.e., ~3.5 mA at higher potential values recorded for MoO_xS_y-CoPi nanoflowers composite

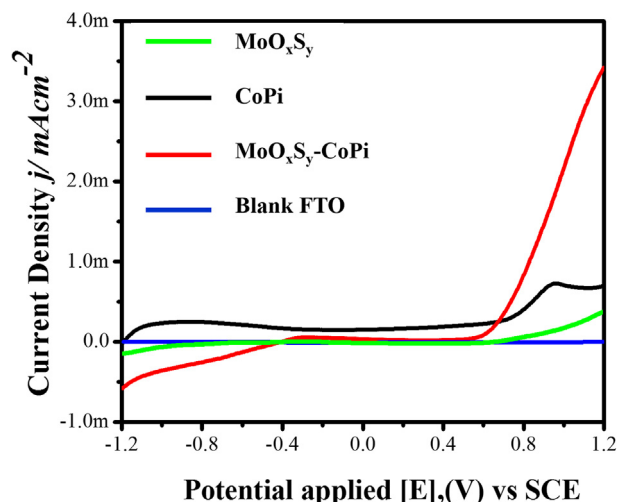


Fig. 8. Linear sweep voltammograms of blank FTO, MoO_xS_y/FTO, CoPi/FTO, and MoO_xS_y-CoPi/FTO photocatalysts at applied potential range of -1.20 V to 1.20 V under 1 SUN solar light in 0.5 M Na₂SO₄ electrolyte (pH 7).

material. The morphology, reduced bandgap, and facile synthetic strategy are advantageous features of our approach that we have implemented in the fabrication of MoO_xS_y-CoPi nanoflowers composites to substantiate better PEC properties.

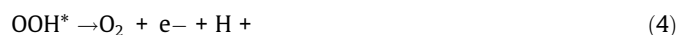
Linear sweep voltammetry (LSV)

Fig. 8 shows a linear sweep voltammetry measurement of MoO_xS_y-CoPi, MoO_xS_y, CoPi, and blank FTO substrate, respectively. The measurement cell is developed by a standard three-electrode configuration using 0.5 M Na₂SO₄ electrolyte at pH 7. The potential range is selected between for -1.20 V to 1.20 V versus SCE under simulated solar light (1 SUN) at a scan rate of 100 mV/Sec. Fig. 8 shows that the pristine MoO_xS_y and CoPi photoelectrodes bear very low current density. In contrast, the enhanced current density of ~0.6 mA/cm² is observed for MoO_xS_y-CoPi nanoflowers composite corresponding to a hydrogen evolution reaction (HER), which is 3–4 times more when compared with a current density of CoPi (~0.15 mA/cm²) and MoO_xS_y material. While looking at a positive potential, the oxygen evolution reaction (OER) is more preferred, and we observed a photocurrent density of ~ 3.5 mA/cm² from MoO_xS_y-CoPi. Whereas, the photocurrent density from CoPi and MoO_xS_y is recorded around ~0.5 and 0.12 mA/cm², respectively. Besides this, we tested blank FTO under 1 SUN solar simulated light. The photoresponse of blank FTO is negligible during LSV measurements for the same selected potential range of -1.20 V to 1.20 V. In overall LSV experiments, we observed dominance of OER by MoO_xS_y-CoPi. It endorses photochemical oxygen evolution preference of MoO_xS_y-CoPi nanoflowers composite material. Hence, these PEC characteristics are the most important achievements acclaimed. Which further supports our *in-situ* impregnation strategy of co-catalyst CoPi in growing MoO_xS_y nanoflowers via facile hydrothermal approach. Consequently, we also observed better morphology, crystallinity, improved optical properties, and excellent photocatalyst current efficiencies. The curved morphology in nanopetals of MoO_xS_y-CoPi helped in better electron mobility and marginal electron-hole recombination[11,63].

MoO_xS_y-CoPi charge transfer mechanism

Fig. 9 explains the most plausible charge transfer mechanism that systematically based on improved interfacial hole transfer in-between FTO substrate and material. The integration of CoPi in MoO_xS_y resulted in suppressing the electron-hole recombination within MoO_xS_y-CoPi composite material [60]. As holes are serving oxygen evolution from water, therefore improved oxidation or OER is observed in comparison to reduction or HER processes from as

engineered MoO_xS_y-CoPi photocatalyst in solar-driven water splitting. “Furthermore, significant photocurrent densities as a result of CoPi incorporation are observed. CoPi is a well-known co-catalyst used for charge separating networks at the catalyst’s interface. Literature revealed that an oxygen evolution catalyst like Co-Pi can catalyze the water electrolysis process to succeed at a low overpotential by changing the reaction pathway [64,65]. When it combines with the MoO_xS_y, the Co-Pi uses the valence band photo holes of the metal oxides/oxysulphide to initiate multiple catalytic reactions [66]. This is accompanied by fast output of photoholes from metal oxide/ oxysulphide to water molecule and undergoes water oxidation. Thus, the relieved charge accumulation at the electrode/electrolyte decreases the electron-hole recombination rate and leads to enhanced photo electrochemical performance. It is also known that additional band bending at the electrode/electrolyte interface may possibly be created by the Co-Pi catalyst, which can also reduce the surface charge recombination [66]. Thermodynamic studies further explained that one-photon and one electron charge separation of photocatalyst is accommodated by the co-catalyst to attain four equivalent electron/hole processes (as shown below), which resulted in enhanced photoresponse during solar-driven water splitting by MoO_xS_y-CoPi photocatalyst [9,29,67].



(where* represents, the active surface sites where OH and O species can interact during PEC-WS process)

These observations indicate better PEC-WS recital of MoO_xS_y-CoPi nanoflowers composite material. Where MoO_xS_y showed effective light sensitivity by the integration of CoPi with it via a hydrothermal approach that ultimately resulted in improved photocurrent densities [9,29,67]. These observations indicate better PEC-WS recital of MoO_xS_y-CoPi nanoflowers composite material. Where MoO_xS_y showed effective light sensitivity by the integration of CoPi with it via a hydrothermal approach that ultimately resulted in improved photocurrent densities.

Conclusion and future perspectives.

Herein, we presented a facile synthesis, characterization, and PEC-WS of novel MoO_xS_y-CoPi photocatalyst. The key features of our strategy include in situ hydrothermal reactions between CoPi and growing MoO_xS_y nanoflowers. The MoO_xS_y-CoPi photocatalyst showed enhanced PEC-WS properties in comparison to bare CoPi and MoO_xS_y. XRD studies of MoO_xS_y-CoPi photocatalyst and CoPi materials confirm orthorhombic crystalline phases. However, XPS analysis predicted the most plausible elemental states of each constituent present in MoO_xS_y-CoPi photocatalyst. The FTIR and Raman spectroscopy’s further comprehended its XRD findings by identifying specific fingerprint regions for particular elements and groups present in the photocatalyst. The results of XPS and Raman are supported by HR-TEM, which confirms the successful incorporation of CoPi into the flakes of MoO_xS_y nanoflowers in the MoO_xS_y-CoPi nanocomposite. FE-SEM studies revealed nanoflowers like morphology showing curved nanopetals with the thickness (≥10 nm) and variable internal spaces (200–400 nm). The comparable optical properties, i.e., diffused reflectance spectroscopy, showed a variation in band-gap energy (2.44 eV) for MoO_xS_y-CoPi compared to bare MoO_xS_y and CoPi. The MoO_xS_y-CoPi/FTO showed significant photocurrent density in

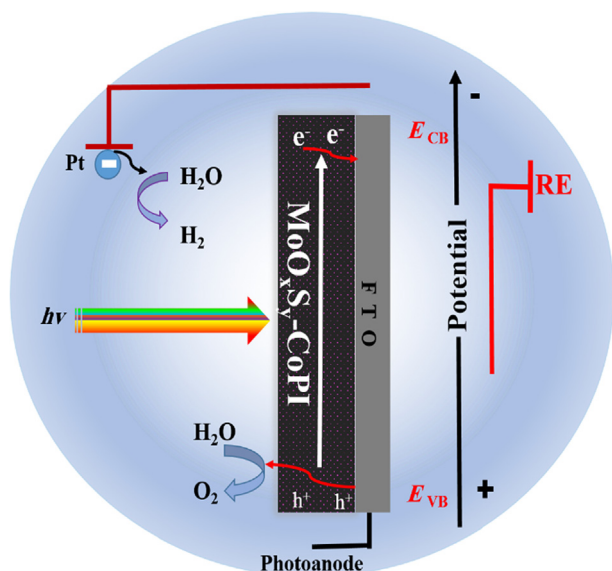


Fig. 9. Energy diagram of MoO_xS_y-CoPi nanoflowers composite material (in 0.5 M Na₂SO₄ at pH 7) coated on FTO glass substrate showing plausible charge transfer mechanism upon exposure to 1 SUN (100mWcm⁻²AM 1.5G) irradiation source.

comparison to $\text{MoO}_x\text{S}_y/\text{FTO}$ and CoPi/FTO . The positive photocurrent is related to photoinduced oxygen evolution reaction (OER). The enhancement of the photocurrent in the case of $\text{MoO}_x\text{S}_y\text{-CoPi}$ is attributed to the improved charge separation and transfer, low electron-hole recombination, photo corrosion stability, and better reaction kinetics. Henceforth, $\text{MoO}_x\text{S}_y\text{-CoPi}$ nanocomposite is considered as a promising material for solar-driven applications. Nonetheless, its PEC-WS and optoelectrical characteristic can be further tuned by doping it with different transition metals or co-catalysts. Thus, the $\text{MoO}_x\text{S}_y\text{-CoPi}$ nanoflowers composite material is a potential candidate to target efficient solar-driven water splitting reactions in similar energy harnessing applications.

Compliance with Ethics Requirements

This article does not contain any studies with human or animal subjects.

Declaration of Competing Interest

The authors declare that they have no known competing financial interests or personal relationships that could have appeared to influence the work reported in this paper.

Acknowledgments

Naseer Iqbal and Asghar Ali extend appreciation to Deanship of Scientific Research (DSR) University of Hafr Al Batin, Saudi Arabia, for supporting them via Research Group Grant Project # G-118-2020.

The authors greatly acknowledge the Center of Research Excellence in Nanotechnology, King Fahd University of Petroleum and Minerals (KFUPM), Dhahran, Saudi Arabia, for experimental and characterization support.

Appendix A. Supplementary data

Supplementary data to this article can be found online at <https://doi.org/10.1016/j.jare.2021.08.006>.

References

- Shi X, Jeong H, Oh SJ, Ma M, Zhang K, Kwon J, et al. Unassisted photoelectrochemical water splitting exceeding 7% solar-to-hydrogen conversion efficiency using photon recycling. *Nat Commun* 2016;7(1):11943.
- Pan Q, Li A, Zhang Y, Yang Y, Cheng C. Rational Design of 3D Hierarchical Ternary $\text{SnO}_2/\text{TiO}_2/\text{BiVO}_4$ Arrays Photoanode toward Efficient Photoelectrochemical Performance. *Adv Sci* 2020;7(3):1902235.
- Wang Y, Tian W, Chen C, Xu W, Li L. Tungsten Trioxide Nanostructures for Photoelectrochemical Water Splitting: Material Engineering and Charge Carrier Dynamic Manipulation. *Adv Funct Mater* 2019;29(23):1809036.
- Fujishima A, Honda K. Electrochemical photolysis of water at a semiconductor electrode. *Nature* 1972;238(5358):37–8.
- Inoue T, Fujishima A, Konishi S, Honda K. Photoelectrocatalytic reduction of carbon dioxide in aqueous suspensions of semiconductor powders. *Nature* 1979;277(5698):637–8.
- Lewis NS, Nocera DG. Powering the planet: Chemical challenges in solar energy utilization. *Proc Natl Acad Sci* 2006;103(43):15729–35.
- Zhen C, Chen R, Wang L, Liu G, Cheng H-M. Tantalum (oxy) nitride based photoanodes for solar-driven water oxidation. *J Mater Chem A* 2016;4(8):2783–800.
- Lee SA, Choi S, Kim C, Yang JW, Kim SY, Jang HW. Si-based water oxidation photoanodes conjugated with earth-abundant transition metal-based catalysts. *ACS Materials Letters* 2019;2(1):107–26.
- Wu X, Zhu C, Wang L, Guo S, Zhang Y, Li H, et al. Control strategy on two-/four-electron pathway of water splitting by multidoped carbon based catalysts. *ACS Catal* 2017;7(3):1637–45.
- Bao J. Recent developments in photocatalytic solar water splitting. *Mater Today* 2014;17(5):208–9.
- Ai G, Mo R, Li H, Zhong J. Cobalt phosphate modified TiO_2 nanowire arrays as co-catalysts for solar water splitting. *Nanoscale* 2015;7(15):6722–8.
- Li Y, Sun Y, Qin Y, Zhang W, Wang L, Luo M, et al. Recent Advances on Water-Splitting Electrocatalysis Mediated by Noble-Metal-Based Nanostructured Materials. *Adv Energy Mater* 2020:1903120.
- Kment Š, Sivula K, Naldoni A, Sarmah SP, Kmentová H, Kulkarni M, et al. FeO-based nanostructures and nanohybrids for photoelectrochemical water splitting. *Prog Mater Sci* 2020;110:100632.
- Zhu L, Hong M, Ho GW. Fabrication of wheat grain textured TiO_2/CuO composite nanofibers for enhanced solar H_2 generation and degradation performance. *Nano Energy* 2015;11:28–37.
- Khan I, Qurashi A, Berdiyev G, Iqbal N, Fuji K, Yamani ZH. Single-step strategy for the fabrication of GaON/ZnO nanoarchitected photoanode their experimental and computational photoelectrochemical water splitting. *Nano Energy* 2018;44:23–33.
- Nishimae S, Mishima Y, Nishiyama H, Sasaki Y, Nakabayashi M, Inoue Y, et al. Fabrication of BaTaO_2N Thin Films by Interfacial Reactions of $\text{BaCO}_3/\text{Ta}_3\text{N}_5$ Layers on a Ta Substrate and Resulting High Photoanode Efficiencies During Water Splitting. *Solar RRL* 2020;4(4):1900542.
- Cheng W-H, Richter MH, May MM, Ohlmann J, Lackner D, Dimroth F, et al. Monolithic Photoelectrochemical Device for Direct Water Splitting with 19% Efficiency. *ACS Energy Lett* 2018;3(8):1795–800.
- Qin P, Fang G, Ke W, Cheng F, Zheng Q, Wan J, et al. In situ growth of double-layer $\text{MoO}_3/\text{MoS}_2$ film from MoS_2 for hole-transport layers in organic solar cell. *J Mater Chem A* 2014;2(8):2742–56.
- Du H, Liu D, Li M, Al Otaibi RL, Lv R, Zhang Y. Solvothermal synthesis of MoS_2 nanospheres in DMF-water mixed solvents and their catalytic activity in hydrocracking of diphenylmethane, RSC. *Advances* 2015;5(97):79724–8.
- Ou NC, Preradovic K, Ferenczy ET, Sparrow CB, Germaine IM, Jurca T, et al. Synthesis and Evaluation of Molybdenum Imido-Thiolato Complexes for the Aerosol-Assisted Chemical Vapor Deposition of Nitrogen-Doped Molybdenum Disulfide. *Organometallics* 2020.
- Li H, Wu J, Yin Z, Zhang H. Preparation and applications of mechanically exfoliated single-layer and multilayer MoS_2 and WSe_2 nanosheets. *Acc Chem Res* 2014;47(4):1067–75.
- Sinha S, Jyotsna SK, Arora, van der Waals Heterostructures based on Liquid Phase Exfoliated MoS_2 and WS_2 nanosheets. *Mater Today: Proc* 2020;21:1840–5.
- Sadler EC, Kempa TJ. Chalcogen Incorporation Process During High Vacuum Conversion of Bulk Mo-oxides to Mo-dichalcogenides. *ACS Applied Electronic Materials* 2020.
- Bao X-Q, Petrovykh DY, Alpuim P, Stroppa DG, Guldris N, Fonseca H, et al. Amorphous oxygen-rich molybdenum oxysulfide decorated p-type silicon microwave arrays for efficient photoelectrochemical water reduction. *Nano Energy* 2015;16:130–42.
- Mukherjee S, Maiti R, Midya A, Das S, Ray SK. Tunable direct bandgap optical transitions in MoS_2 nanocrystals for photonic devices. *ACS Photonics* 2015;2(6):760–8.
- NJ. Mayhall, I.I.E.L. Becher, A. Chowdhury, K. Raghavachari, Molybdenum Oxides versus Molybdenum Sulfides: Geometric and Electronic Structures of Mo_3X_y (X = O, S and y = 6, 9) Clusters, *The Journal of Physical Chemistry A* 115(11) (2011) 2291–2296.
- Sinain H, Ham DJ, Lee JS, Phuruangrat A, Thongtem S, Thongtem T. Free-polymer controlling morphology of $\alpha\text{-MoO}_3$ nanobelts by a facile hydrothermal synthesis, their electrochemistry for hydrogen evolution reactions and optical properties. *J Alloy Compd* 2012;516:172–8.
- Xie J, Zhang J, Li S, Grote F, Zhang X, Zhang H, et al. Controllable Disorder Engineering in Oxygen-Incorporated MoS_2 Ultrathin Nanosheets for Efficient Hydrogen Evolution. *J Am Chem Soc* 2013;135(47):17881–8.
- Liao J, Sa B, Zhou J, Ahuja R, Sun Z. Design of high-efficiency visible-light photocatalysts for water splitting: MoS_2/AlN (GaN) heterostructures. *The Journal of Physical Chemistry C* 2014;118(31):17594–9.
- Gao C, Hua H, Du M, Liu J, Wu X, Pu Y, Xa. Li, 1T/2H MoS_2 nanoflowers decorated amorphous Mo-CoS_x skeleton: A ZIF-based composite electrocatalyst for the hydrogen evolution reaction. *Appl Surf Sci* 2020;515:145842.
- Xie J, Zhang H, Li S, Wang R, Sun X, Zhou M, et al. Defect-Rich MoS_2 Ultrathin Nanosheets with Additional Active Edge Sites for Enhanced Electrocatalytic Hydrogen Evolution. *Adv Mater* 2013;25(40):5807–13.
- Huang D, Chen S, Zeng G, Gong X, Zhou C, Cheng M, et al. Artificial Z-scheme photocatalytic system: What have been done and where to go? *Coord Chem Rev* 2019;385:44–80.
- Yoon S-H, Sadike T, Ding J-R, Kim K-S. Photoelectrochemical oxygen evolution with cobalt phosphate and BiVO_4 modified 1-D WO_3 prepared by flame vapor deposition. *J Ind Eng Chem* 2020.
- McDonald JW, Friesen GD, Rosenhein LD, Newton WE. Syntheses and characterization of ammonium and tetraalkylammonium thiomolybdates and thiotungstates. *Inorg Chim Acta* 1983;72:205–10.
- Genuit D, Bezverkhyy I, Afanasiev P. Solution preparation of the amorphous molybdenum oxysulfide MoOS_2 and its use for catalysis. *J Solid State Chem* 2005;178(9):2759–65.
- Zhou G, Wang W, Gu G, Li Y, Liu Y. Microwave assisted synthesis of cobalt phosphate nanoparticles and their antiproliferation against human lung cancer cells and primary osteoblasts in vitro. *Int J Chem* 2011;3(4):127.
- Huang X, Ma J, Wu P, Hu Y, Dai J, Zhu Z, et al. Hydrothermal synthesis of LiCoPO_4 cathode materials for rechargeable lithium ion batteries. *Mater Lett* 2005;59(5):578–82.

- [38] Shannon RD. Revised effective ionic radii and systematic studies of interatomic distances in halides and chalcogenides. *Acta crystallographica section A: crystal physics, diffraction, theoretical and general crystallography* 1976;32(5):751–67.
- [39] Naouel R, Dhaouadi H, Touati F, Gharbi N. Synthesis and Electrical Properties of Well-Ordered Layered α -MoO₃ Nanosheets. *Nano-Micro Letters* 2011;3(4):242–8.
- [40] Benoist L, Gonbeau D, Pfister-Guillouzo G, Schmidt E, Meunier G, Levasseur A. X-ray photoelectron spectroscopy characterization of amorphous molybdenum oxysulfide thin films. *Thin Solid Films* 1995;258(1):110–4.
- [41] Deroide B, Belougne P, Zanchetta JV. Etude par resonance paramagnetique electronique de sulfures de molybdene et de tungstene. *J Phys Chem Solids* 1987;48(12):1197–205.
- [42] Deroide B, Bensimon Y, Belougne P, Zanchetta JV. Lineshapes of ESR signals and the nature of paramagnetic species in amorphous molybdenum sulfides. *J Phys Chem Solids* 1991;52(7):853–7.
- [43] McIntyre N, Cook M. X-ray photoelectron studies on some oxides and hydroxides of cobalt, nickel, and copper. *Anal Chem* 1975;47(13):2208–13.
- [44] Tan BJ, Klabunde KJ, Sherwood PM. XPS studies of solvated metal atom dispersed (SMAD) catalysts. Evidence for layered cobalt-manganese particles on alumina and silica, *Journal of the American Chemical Society* 1991;113(3):855–61.
- [45] Carver J, Schweitzer G, Carlson TA. Use of X-Ray photoelectron spectroscopy to study bonding in Cr, Mn, Fe, and Co compounds, *The Journal of Chemical Physics* 1972;57(2):973–82.
- [46] J. Bonnelle, J. Grimblot, A. D'huysser, Influence de la polarisation des liaisons sur les spectres esca des oxydes de cobalt, *Journal of Electron Spectroscopy and Related Phenomena* 7(2) (1975) 151-162.
- [47] Ferrigna C, Massucci M. Inclusion Phenom. *Mol Recogn Chem* 1989;7:529.
- [48] E. Fluck, D. Weber, P2P binding-energies in phosphorus (III) compounds, phosphonium salts and oxyacids of phosphorus, *ZEITSCHRIFT FÜR NATURFORSCHUNG SECTION BA JOURNAL OF CHEMICAL SCIENCES* (9-10) (1974) 603-607.
- [49] An L, Huang L, Zhou P, Yin J, Liu H, Xi P. A Self-Standing High-Performance Hydrogen Evolution Electrode with Nanostructured NiCo₂O₄/CuS Heterostructures. *Adv Funct Mater* 2015;25(43):6814–22.
- [50] Suryanto BH, Lu X, Chan HM, Zhao C. Controlled electrodeposition of cobalt oxides from protic ionic liquids for electrocatalytic water oxidation. *RSC Adv* 2013;3(43):20936–42.
- [51] Tauc J. Optical properties and electronic structure of amorphous Ge and Si. *Mater Res Bull* 1968;3(1):37–46.
- [52] Stenzel O. *The physics of thin film optical spectra*. Springer; 2015.
- [53] Downes CA, Marinescu SC. Efficient electrochemical and photoelectrochemical H₂ production from water by a cobalt dithiolene one-dimensional metal-organic surface. *J Am Chem Soc* 2015;137(43):13740–3.
- [54] Wang W, Zheng B, Liu Z, Zhou G. MICROWAVE ASSISTED SYNTHESIS OF COBALT PHOSPHATE NANOPARTICLES. *European Chemical Bulletin* 2014;3(5):485–8.
- [55] Casadio F, Bezúr A, Fiedler I, Muir K, Trad T, Maccagnola S. Pablo Picasso to Jasper Johns: a Raman study of cobalt-based synthetic inorganic pigments. *J Raman Spectrosc* 2012;43(11):1761–71.
- [56] Nagaraju G, Tharamani C, Chandrappa G, Livage J. Hydrothermal synthesis of amorphous MoS₂ nanofiber bundles via acidification of ammonium heptamolybdate tetrahydrate. *Nanoscale Res Lett* 2007;2(9):461–8.
- [57] Zhang ZJ, Zhang J, Xue QJ. Synthesis and Characterization of a Molybdenum Disulfide Nanocluster. *The Journal of Physical Chemistry* 1994;98(49):12973–7.
- [58] Tsyganenko AA, Can F, Travert A, Maugé F. FTIR study of unsupported molybdenum sulfide—in situ synthesis and surface properties characterization. *Appl Catal A* 2004;268(1–2):189–97.
- [59] Liu Shasha, Zhang Xuebin, Shao Hao, Xu Jie, Chen Fanyan, Feng Yi. Preparation of MoS₂ nanofibers by electrospinning. *Mater Lett* 2012;73:223–5.
- [60] Tian J, Li H, Asiri AM, Al-Youbi AO, Sun X. Photoassisted preparation of cobalt phosphate/graphene oxide composites: a novel oxygen-evolving catalyst with high efficiency. *small* 2013;9(16):2709–14.
- [61] Li H, Zhang Q, Yap CCR, Tay BK, Edwin THT, Olivier A, et al. From bulk to monolayer MoS₂: evolution of Raman scattering. *Adv Funct Mater* 2012;22(7):1385–90.
- [62] Eda G, Yamaguchi H, Voiry D, Fujita T, Chen M, Chhowalla M. Photoluminescence from chemically exfoliated MoS₂. *Nano Lett* 2011;11(12):5111–6.
- [63] Barroso M, Cowan AJ, Pendlebury SR, Grätzel M, Klug DR, Durrant JR. The role of cobalt phosphate in enhancing the photocatalytic activity of α -Fe₂O₃ toward water oxidation. *J Am Chem Soc* 2011;133(38):14868–71.
- [64] Ai G, Mo R, Li H, Zhong J. Cobalt phosphate modified TiO₂ nanowire arrays as co-catalysts for solar water splitting. *Nanoscale* 2015;7(15):6722–8.
- [65] Li P, Jin Z, Xiao D. A one-step synthesis of Co–P–B/rGO at room temperature with synergistically enhanced electrocatalytic activity in neutral solution. *J Mater Chem A* 2014;2(43):18420–7.
- [66] Zhang Z, Yates Jr JT. Band bending in semiconductors: chemical and physical consequences at surfaces and interfaces. *Chem Rev* 2012;112(10):5520–51.
- [67] Pandey LB, Aikens CM. Theoretical investigation of the electrochemical mechanism of water splitting on a titanium oxide cluster model. *The Journal of Physical Chemistry A* 2012;116(1):526–35.